



Full paper

A fundamental understanding of the Fe/Ti doping induced structure formation process to realize controlled synthesis of layer-tunnel $\text{Na}_{0.6}\text{MnO}_2$ cathode

Dong Wang^a, Chenguang Shi^b, Ya-Ping Deng^c, Zhenguo Wu^{a,**}, Zuguang Yang^a, Yanjun Zhong^a, Yi Jiang^c, Benhe Zhong^a, Ling Huang^b, Xiaodong Guo^{a,d}, Zhongwei Chen^{c,*}

^a College of Chemical Engineering, Sichuan University, Chengdu, 610065, PR China

^b College of Chemistry and Chemical Engineering, Xiamen University, Xiamen, 361005, PR China

^c Department of Chemical Engineering, University of Waterloo, Waterloo, ON, N2L 3G1, Canada

^d Institute for Superconducting and Electronic Materials, University of Wollongong, Wollongong, NSW, 2522, Australia



ARTICLE INFO

Keywords:

Sodium-ion batteries
Cathode
Composite structure
Layer-tunnel
Formation process

ABSTRACT

It's well known that ion-doping could modify the crystal structure and adjust the corresponding performance of cathode, but how the doped ions affect the structure formations during high-temperature calcination still remains a daunting challenge, which is critical for the ideal controlled synthesis. In our previous study, we have found that the cationic ion doping can both tune the single phase structure and adjust the phase ratio in layer-tunnel $\text{Na}_{0.6}\text{MnO}_2$. And in the present study, we furtherly try to track the influence of varied Fe^{3+} and Ti^{4+} on the formation process of layer-tunnel hybrid structures and focus on the thermal behavior, structure evolution and morphology change. The kinetics-preferred layered structure can be detected at the initial stage and transfer to the thermodynamic-stable tunnel structure at increased temperature. The Fe^{3+} can stabilize the formed layer structure while the Ti^{4+} promote the latter transformation. More interesting, the Ti^{4+} plays a dominant role when $\text{Fe}^{3+}/\text{Ti}^{4+}$ were co-doped. The impressive results can be related with the more orderly structure of layer phase and distorted coordination in tunnel phase. This research correlates the synthesis process and the final structure, as well as the ultimate electrochemical performance, which shed new light on the development of advanced oxides cathode.

1. Introduction

Layered oxides cathode has attracted great attentions in both lithium ion batteries (LIBs) and sodium ion batteries (SIBs) [1–5]. And ion-doping strategy has been widely adopted and extensively studied in developing high performance cathode [6–10]. However, the previous reports mainly focused on the crystal structure modification, suppressed phase transformation during charge/discharge and enhanced thermal stability of the doped samples [11,12]. The investigations go deep into the ion-doping process, the phase transformation, structure formation and morphology change during synthesis process were neglected.

Recently, the detailed synthesis process of layered oxides cathode of LIBs during high-temperature calcination has attracted increasing efforts. And the results provide significant value to realize the controlled

synthesis [13]. Hua et al. [14] had an in-depth study on the structure transformation of Li-Rich Layered $\text{Li}[\text{Li}_{0.2}\text{Ni}_{0.2}\text{Mn}_{0.6}]\text{O}_2$ during microwave calcination, indicating that the electrochemical properties of cathode materials are closely related to the phase composition and synthesis procedure. Wang et al. [15] found that calcination temperature had a great influence on the cationic ordering in layered $\text{LiNi}_{0.7}\text{Mn}_{0.15}\text{Co}_{0.15}\text{O}_2$. Through the synthesis control of the kinetic reaction pathway during high-temperature calcination, even in air, the highly ordered $\text{LiNi}_{0.7}\text{Mn}_{0.15}\text{Co}_{0.15}\text{O}_2$ cathode material was tuned for excellent electrochemical properties. As a promising candidate of SIBs, the layer-based composite cathodes (P2/P3 [16–18], P2/O3 [19–21], P2/tunnel [22,23] etc.) display integrated advantages of the combined pure phase [24,25]. And the complicated structure evolution occurs during high-temperature solid state reaction highly demand detailed

* Corresponding author.

** Corresponding author.

E-mail address: zhwchen@uwaterloo.ca (Z. Chen).

<https://doi.org/10.1016/j.nanoen.2020.104539>

Received 11 November 2019; Received in revised form 14 January 2020; Accepted 26 January 2020

Available online 29 January 2020

2211-2855/© 2020 Elsevier Ltd. All rights reserved.

exploration. In 2017, Khalil Amine et al. [26] conducted in-operando synchrotron HEXRD on the materials after pre-calcining and to detect the phase transition of P2/O3/O1 composite materials. By quenching the materials at different temperature in air, a series of composite materials with outstanding properties were prepared.

Meanwhile, to our best knowledge, there was almost no particular research on the influence of different transition metal ions on the evolution of composite structures during high temperature solid state reaction. Moreover, the involved chemical bond reconstruction, ion migration and phase evolution are fundamental and crucial for the investigation of synergistic mechanism and designing advanced composite materials. In our previous study, we have concluded the enhanced performance of layer-tunnel composite cathode and the phase ratio modification effect of some doped ions [27,28]. However, the functional mechanism of introduced ions remains unclear.

In this work, environmentally friendly Fe^{3+} and Ti^{4+} were selected as probe to clarify the doping effect during the calcination process with the help of some in-situ/ex-situ characterization techniques and DFT calculation. The $\text{Na}_{0.7}\text{FeO}_2/\text{NaFeO}_2$ are layered structure, while $\text{Na}_4\text{Mn}_4\text{Ti}_5\text{O}_9$ is an isomorphous structure with tunnel structure [12,23]. The results show that Fe^{3+} (Ti^{4+}) can induce the selective formation of layer (tunnel) structure during high-temperature treatment, respectively. A step further, the Ti^{4+} played the dominant role when $\text{Ti}^{4+}/\text{Fe}^{3+}$ co-doped, which was also confirmed via DFT calculation. After a systematic optimization, the $\text{Na}_{0.6}\text{Mn}_{0.9}\text{Ti}_{0.1}\text{O}_2$ shows the balanced cycling stability and rate performance. The above results can be used to formulate rational strategies to develop high performance electrode.

2. Material preparation

All series of layer/tunnel composite materials ($\text{Na}_{0.60}\text{Mn}_{1-x-y}\text{Fe}_x\text{Ti}_y\text{O}_2$, $x = 0, 0.05, 0.1$, $y = 0, 0.05, 0.1$, namely $\text{Na}_{0.60}\text{MnO}_2$, $\text{Na}_{0.60}\text{Mn}_{0.95}\text{Fe}_{0.05}\text{O}_2$, $\text{Na}_{0.60}\text{Mn}_{0.90}\text{Fe}_{0.10}\text{O}_2$, $\text{Na}_{0.60}\text{Mn}_{0.95}\text{Ti}_{0.05}\text{O}_2$, $\text{Na}_{0.60}\text{Mn}_{0.90}\text{Ti}_{0.10}\text{O}_2$, $\text{Na}_{0.60}\text{Mn}_{0.90}\text{Fe}_{0.05}\text{Ti}_{0.05}\text{O}_2$ and $\text{Na}_{0.60}\text{Mn}_{0.80}\text{Fe}_{0.10}\text{Ti}_{0.10}\text{O}_2$, marked as MFT0, MF5, MF10, MT5, MT10, MFT5 and MFT10) samples were synthesized by co-precipitation method and high-temperature solid-state reaction. The stoichiometric amounts $\text{CH}_3\text{COONa}\cdot 3\text{H}_2\text{O}$ (2% excess $\text{CH}_3\text{COONa}\cdot 3\text{H}_2\text{O}$ was added to make up the volatilization of Na during high-temperature calcination), Mn ($(\text{CH}_3\text{COOH})_2\cdot 4\text{H}_2\text{O}$, TiO_2 (insoluble in deionized water) and Fe ($(\text{NO}_3)_3\cdot 9\text{H}_2\text{O}$ (All reagents were Analytical-reagent-grade) were dissolved in 100 mL of deionized water. Then, the $\text{H}_2\text{C}_2\text{O}_4\cdot 2\text{H}_2\text{O}$ aqueous solution as precipitant was added slowly under vigorous stirring at 40°C for 3 h. Extra water was evaporated at 90°C to obtain a milky white precursor. After drying at 100°C for 12 h, the precursor was pre-annealed at 450°C for 6 h with the heating rate of $5^\circ\text{C}/\text{min}$ and

following high-temperature calcination at 800°C for 12 h in air. Finally, the prepared sample was naturally cooled to room temperature and stored in an Ar-atmosphere glovebox to avoid contacting with air.

3. Results and discussions

3.1. Crystal structure and particle morphology

The as-prepared layer-tunnel composite materials $\text{Na}_{0.60}\text{Mn}_{1-x-y}\text{Fe}_x\text{Ti}_y\text{O}_2$ ($x = 0, 0.05, 0.1$, $y = 0, 0.05, 0.1$) were marked as MFT0 ($\text{Na}_{0.60}\text{MnO}_2$), MF5 ($\text{Na}_{0.60}\text{Mn}_{0.95}\text{Fe}_{0.05}\text{O}_2$), MF10 ($\text{Na}_{0.60}\text{Mn}_{0.90}\text{Fe}_{0.10}\text{O}_2$), MT5 ($\text{Na}_{0.60}\text{Mn}_{0.95}\text{Ti}_{0.05}\text{O}_2$), MT10 ($\text{Na}_{0.60}\text{Mn}_{0.90}\text{Ti}_{0.10}\text{O}_2$), MFT5 ($\text{Na}_{0.60}\text{Mn}_{0.90}\text{Fe}_{0.05}\text{Ti}_{0.05}\text{O}_2$) and MFT10 ($\text{Na}_{0.60}\text{Mn}_{0.80}\text{Fe}_{0.10}\text{Ti}_{0.10}\text{O}_2$) in which M, F and T represent Mn, Fe and Ti, respectively. The diffraction peaks (Fig. 2a) can be assigned to layer structure (space group: $P6_3/mmc$, PDF no. 00-027-0751) [29] and tunnel structure (space group: $Pbam$, PDF no.00-027-0750) [30]. No obvious peaks of tunnel structure can be observed with Fe^{3+} adapted. On the contrary, the intensities of the corresponding peaks become more and more strong with Ti^{4+} . More interestingly, the tunnel structure still possesses the majority position when $\text{Fe}^{3+}/\text{Ti}^{4+}$ were co-doped. The Fe/Ti content of co-doping samples is shown in Table S2. The XRD refinements with reasonable errors were fulfilled to give more reliable and intuitive expression (Fig. 2b). And a continuous component ratio adjustment can be realized via tuning the $\text{Fe}^{3+}/\text{Ti}^{4+}$ content.

Different ratio of typical flake shapes (P2-type phase) and rod-like particles (T-type tunnel phase) could be observed in these composites (Fig. 3a–g). More plate-like particles could be observed with increased Fe^{3+} content. On the contrary, more rod-like particles could be obtained with more Ti^{4+} and simultaneous introduced $\text{Ti}^{4+}/\text{Fe}^{3+}$. The SEM analysis consisted with the XRD results, further confirm it that $\text{Fe}^{3+}/\text{Ti}^{4+}$ were beneficial to the formation of P2 layer/tunnel structure in the final products, respectively. From the EDS-mapping images, the Fe and Ti element show homogeneous distribution on P2 layer/tunnel of MF10 and MT10 samples. TEM was further employed to obtain crystal structure information of the chosen MFT10 sample (Fig. 3h–i). The interplanar distance of 0.249 nm in the plate-like particle corresponds to (100) plane of the P2-type layered structure (Fig. 3h), The lattice fringe of the rod-like particle show a spacing of 0.263 nm, corresponding to (300) plane of the tunnel structure (Fig. 3i). XPS measurement was performed to investigate the valence states of transition metal elements of Mn, Ti and Fe of MTF10 sample. The two peaks at 641.6 eV and 653.9 eV could be assigned to the binding energies of Mn $2p^{3/2}$ and Mn $2p^{1/2}$ with satellite peaks located at 643.4 eV and 652.7 eV, confirming the mixed valences of Mn^{3+} and Mn^{4+} [31,32]. And the Ti $2p^{1/2}$ and Ti $2p^{3/2}$ peaks locate at 463.4 eV and 457.5 eV evidence the Ti^{4+} [33]. In Fig. 3o,

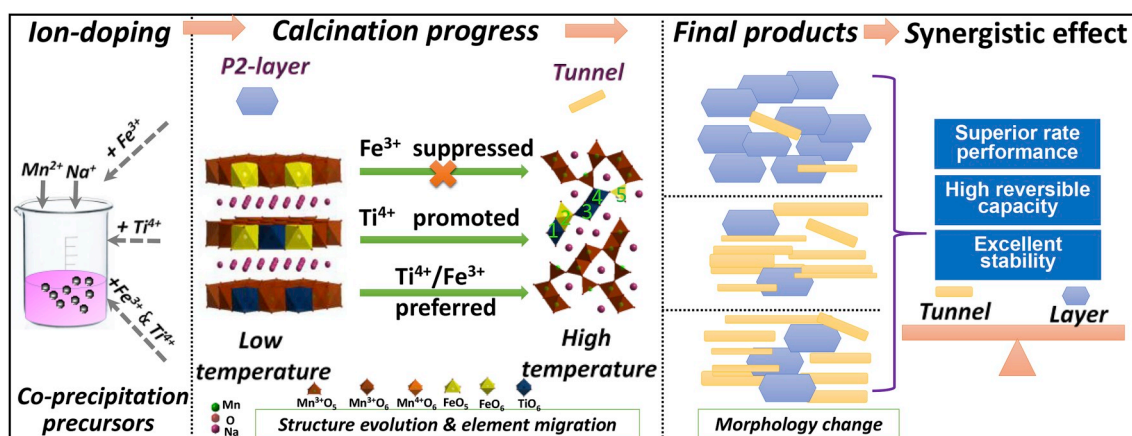


Fig. 1. Schematic illustration the controlled synthesis and the correlation of different ion-doping ($\text{Fe}^{3+}/\text{Ti}^{4+}$), structure formation progress, final products and synergistic effect in P2 layer-tunnel composite structures.

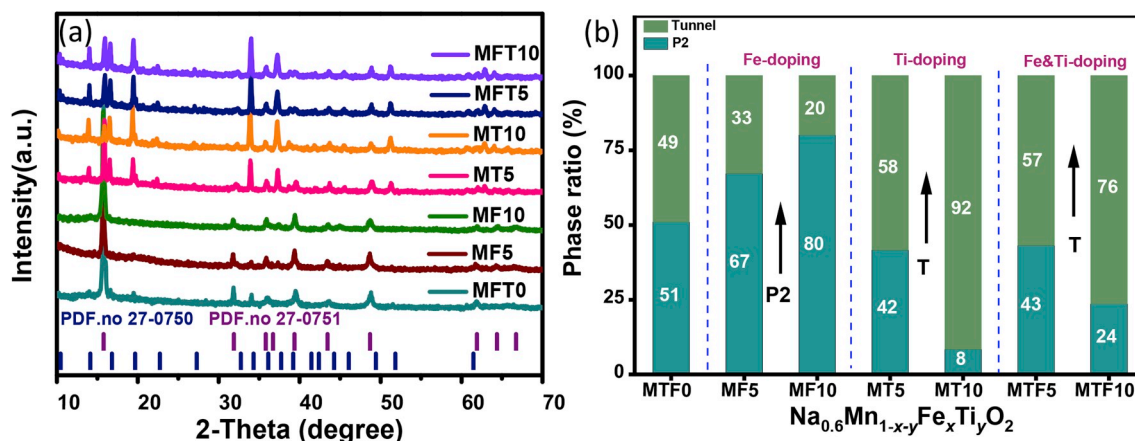


Fig. 2. XRD patterns of materials (a) MFT0 ($\text{Na}_{0.60}\text{MnO}_2$), MF5 ($\text{Na}_{0.60}\text{Mn}_{0.95}\text{Fe}_{0.05}\text{O}_2$), MF10 ($\text{Na}_{0.60}\text{Mn}_{0.90}\text{Fe}_{0.10}\text{O}_2$), MT5 ($\text{Na}_{0.60}\text{Mn}_{0.95}\text{Ti}_{0.05}\text{O}_2$), MT10 ($\text{Na}_{0.60}\text{Mn}_{0.90}\text{Ti}_{0.10}\text{O}_2$), MFT5 ($\text{Na}_{0.60}\text{Mn}_{0.90}\text{Fe}_{0.05}\text{Ti}_{0.05}\text{O}_2$) and MFT10 ($\text{Na}_{0.60}\text{Mn}_{0.80}\text{Fe}_{0.10}\text{Ti}_{0.10}\text{O}_2$). This abbreviation is used in subsequent sections. (b) XRD Rietveld refinements ratio of P2 layer/tunnel phase of all as-prepared samples.

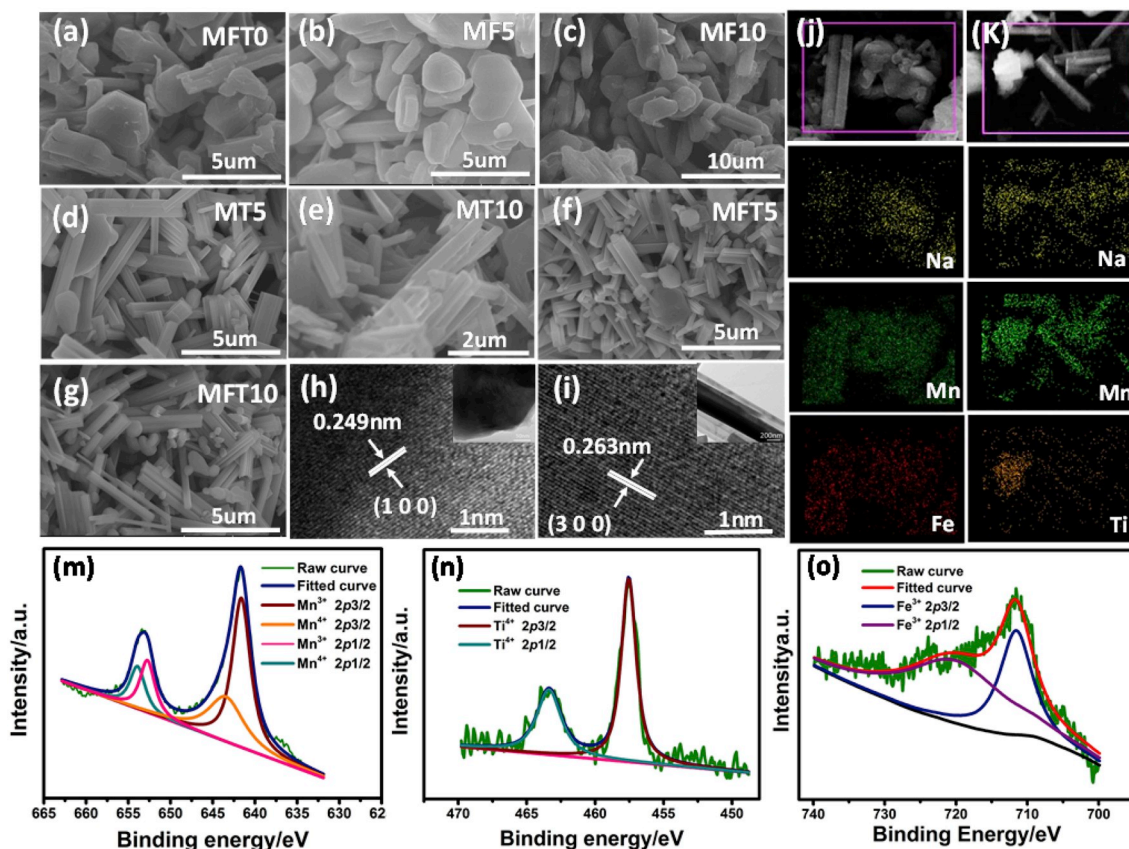


Fig. 3. SEM images of as-prepared samples (a) MFT0, (b) MF5, (c) MF10, (d) MT5, (e) MT10, (f) MFT5 and (g) MFT10. HRTEM images of MFT10 sample (h) P2 layer structure and (i) tunnel structure. EDS-mapping images of samples (j) MF10 (k) MT10. XPS spectrum of the transition metal element of MFT10 sample (m) Mn, (n) Ti and (o) Fe.

the typical coupled peaks at 711.6 eV, 720.3 eV show that the valence state of Fe is +3 [34].

To correlate the thermal reaction behavior of the precursor and the formation process, the TG and DSC tests were performed from room temperature to 800 °C for simulating the material practical calcination conditions including periods of the constant temperature heating (Fig. 4). In step 1, the endothermic peaks and a sharp weight loss occurs in MT10 and MF10 precursor below 250 °C are associated with the removal of absorptive water, crystalline water and residual oxalic acid.

And then the anions continuously decomposed to metal oxides [35]. In step 2, the gradual weight loss in TG curve and endothermic trend of DSC curve suggest a small amount of anion decomposition and formation of oxides at the early stage. As to step 3, obvious weight loss peak and endothermic peak appeared in the DTG/DSC curves of MF10 and MT10, implying that the major solid state reaction including phase transformation occurred in this condition. The weight loss peak and endothermic peak of MF10 with more layered structures appeared at 636 °C and 703 °C, which is lower than that of MT10 contained more

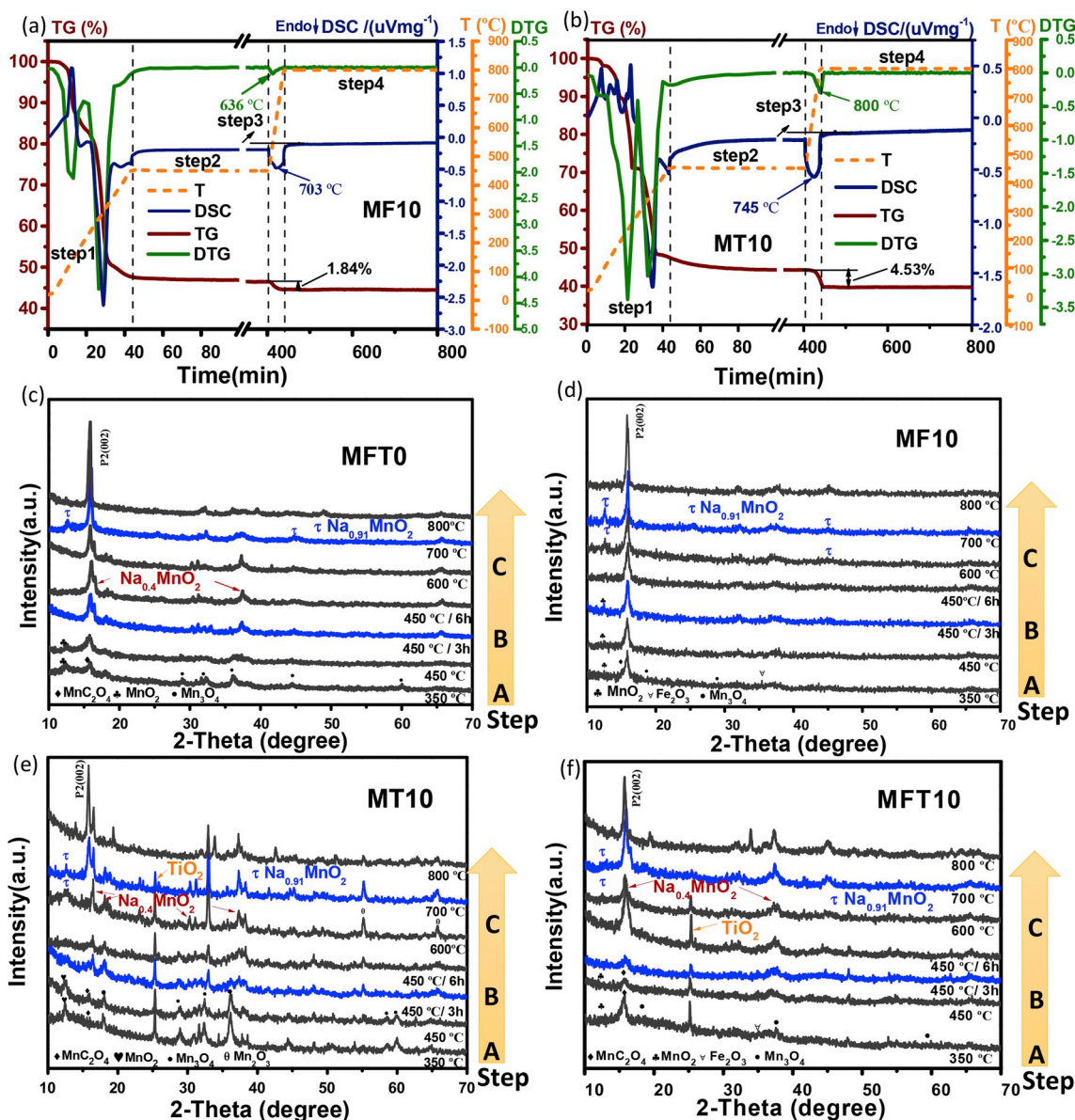


Fig. 4. The TG/DSC/temperature/DTG profiles of (a) MF10 precursor (b) MT10 precursor. The heating stages below 450 °C, 450 °C/0–6 h, 450–800 °C and 800 °C/0–6 h are noted as the step 1, 2, 3 and 4, respectively. (c–f) the ex-situ XRD patterns of MFT0, MF10, MT10 and MFT10 sample at different temperatures during calcination after quenching with liquid nitrogen. The heating stages below 450 °C, 450 °C/0–3–6 h, 450–800 °C are marked as the step A, B and C, respectively.

tunnel (800 °C and 745 °C). Additionally, 1.83% weight loss and 4.53% weight loss can be observed in the TG curves of MT10 and MF10, which were related to the evaporation of Na and O₂ from previous report [36]. The varied thermal behaviors reveal that the layered structure was generated at a lower temperature range than tunnel structure. Finally, the baselines of DSC curves in both MT10 and MF10 shifted up, indicating that the changes of material heat capacity after the important step 3. In the latter step 4, the TG and DSC curves were stable without obvious changes, the layer/tunnel composite structures have been formed with different composition ratios [37].

The ex-/in-situ XRD was conducted to reveal the influence of Fe³⁺/Ti⁴⁺ on layer/tunnel formation process during high-temperature calcination. The ex-situ XRD patterns of MFT0, MF10, MT10 and MFT10 were obtained by quenching the samples with liquid nitrogen at different temperatures (Fig. 4c–f). In step A, the ex-situ XRD results uncover the complex products of the decomposition reaction of oxalate, including manganese oxide (MnO₂/Mn₃O₄), the undecomposed manganese oxalate, TiO₂ in samples MT10/MFT10 (Fig. 4e–f), and a small

amount of Fe₂O₃ in samples MF10/MFT10. In the step B, besides the Mn-based oxides, TiO₂ could be observed in MT10/MFT10 [38]. Meanwhile, the major characteristic (002) peak at ~15.8° of P2 layered structure gradually emerged with iron oxides disappeared. Therefore, the original layer structure formed earlier than tunnel structure, which can be related with the simpler structure and lower formation energy of layer structure. And most Fe³⁺ migrated into the host structure and promoted formation and stability of layer structure in lower temperature range. At the same time, some Na_{0.4}MnO₂ (PDF no. 00-027-0749) with the 2 × 3 tunnels generated in MT10 and disappeared in step D [39]. This intermediate phase may be related with the insufficient migration of Na⁺ into manganese oxides at low temperature range [40,41]. However, Na_{0.4}MnO₂ was almost not detected in MF10 (Fig. 4d), which further demonstrate that Fe³⁺ promoted the formation of layered structure in lower temperature range. In step C, the XRD peaks is assigned to Na_{0.91}MnO₂ (PDF 38-0965) at 600–700 °C and then disappeared in step D can be observed in all the as-prepared samples [42, 43]. And the thermodynamic stable phase in step D (800 °C) is still the

layer/tunnel composite phase with Na/Mn ratio of 0.6 (Fig. 5).

In step D, the continued increasing diffraction intensity and narrowing width of (002) peak correspond to improving crystallization of P2 structure in MFT0, MF10, MT10 and MFT10 (Fig. 5). And the strengthened peaks at $\sim 32.1^\circ$ (004), $\sim 36.0^\circ$ (100), $\sim 37.0^\circ$ (101), $\sim 43.8^\circ$ (103) and $\sim 49.1^\circ$ (104) indicate the crystal growth of layer structure. Moreover, as to MFT0, the characteristic peaks at $\sim 14.0^\circ$ (130), $\sim 16.7^\circ$ (140), $\sim 19.5^\circ$ (200), $\sim 34.1^\circ$ (350), $\sim 37.5^\circ$ (201) and $\sim 51.5^\circ$ (2,10,1) of tunnel structure gradually emerged and strengthened while holding at 800°C , which suggest the transformation from layer to tunnel at high temperature range. For MF10, no obvious peaks belong to tunnel structure can be detect. Inversely, once the Ti^{4+} was introduced (MT10/MFT10), the tunnel structure took the dominant position. It was further shown that the Fe^{3+} could stabilize the initially formed layer structure and suppressed the “layer to tunnel” structure transformation. On the contrary, the introduction of Ti^{4+} highly promoted the structure evolution. The above results reveal detailed phase evolution during calcination. And the layer structure is kinetics-preferred due to the high structural symmetry. And the “layer to tunnel” transformation under high temperature demonstrates the better thermodynamics-stability of tunnel structure, which has been reported in previous investigations [44,45]. Moreover, the relative complex coordination-atmosphere in tunnel structure make it difficult to be formed under low temperature even though with low Na/TM ratio. The Fe^{3+} could stabilize the layer structure at high temperature and suppress the phase transformation. Nevertheless, the existence of Ti^{4+} can dramatically boost the tunnel structure formation.

In-situ high-temperature XRD was conducted on MF10/MT10 after pretreatment (450°C , 6 h) and exhibits similar structure formation process to that of the ex-situ XRD tests. In the initial state ($25\text{--}500^\circ\text{C}$), more layered structure is still formed in MF10 samples after pre-calcination (Fig. 6a), while the layer structure and some tunnel $\text{Na}_{0.4}\text{MnO}_2$ simultaneously formed in MT10 samples (Fig. 6b). In later

stage, most layer structure in MF10 remains in the high-temperature section. However, the layered structure peaks in MT10 gradually weakened while tunnel structure peaks strengthened over 700°C (Fig. 6b and d). The peaks of TiO_2 under low-temperature in MT10 completely vanished in high-temperature range with the dramatically increasing of tunnel structure peaks in high-temperature range, indicating that Ti^{4+} enters the host structure and promoted the transition from the earlier layered structure to tunnel structure. However, Fe^{3+} enters the host structure under low temperature and enhance the thermodynamic stability of layer structure in the later high temperature range. And less layer structures were transformed into tunnel structures with more Fe^{3+} , which results in an increased layered structure proportion in the final products (MF10). Interestingly, when Fe^{3+} was present in the early structure, Ti^{4+} still strongly facilitate the transition from the primary layer structure to the tunnel structure in the high-temperature stage from MFT10 sample. The reasons for structure evolution, including Fe/Ti oxides disappearance and entrance into the host structure at different temperature ranges during calcining, was probably related with the migration energy of different ions [46]. Moreover, considering the crystal coordination sites, the Fe^{3+} was easy to occupy the octahedral sites of the P2 layer structure under low temperature and substitute little Mn^{3+} sites (Mn2/Mn5) of the tunnel structure because of the similar valence states and ionic radii ($\text{Mn}^{3+}/0.645\text{ \AA}$ and $\text{Fe}^{3+}/0.645\text{ \AA}$), resulting in more stable layered structures. On the contrary, the $\text{Na}_{0.44}\text{MnO}_2$ was isostructural with $\text{Na}_4\text{Mn}_4\text{Ti}_5\text{O}_{18}$ [47], in which Ti^{4+} is more likely to occupy the Mn^{4+} sites (Mn1/Mn3/Mn4) [48], which also implies that the increasing Ti^{4+} could promote the formation of tunnel structure. These results were illustrated in Fig. 1 and Fig. 7a–b. The total reaction for the oxalate precursor to obtain P2 layer-tunnel in the calcining stage can be expressed by two reactions (Fig. 7 (1) and (2)). Moreover, the DFT theoretical calculation of the influence different content of $\text{Fe}^{3+}/\text{Ti}^{4+}$ on the layer-tunnel structures will be further explained in the subsequent part.

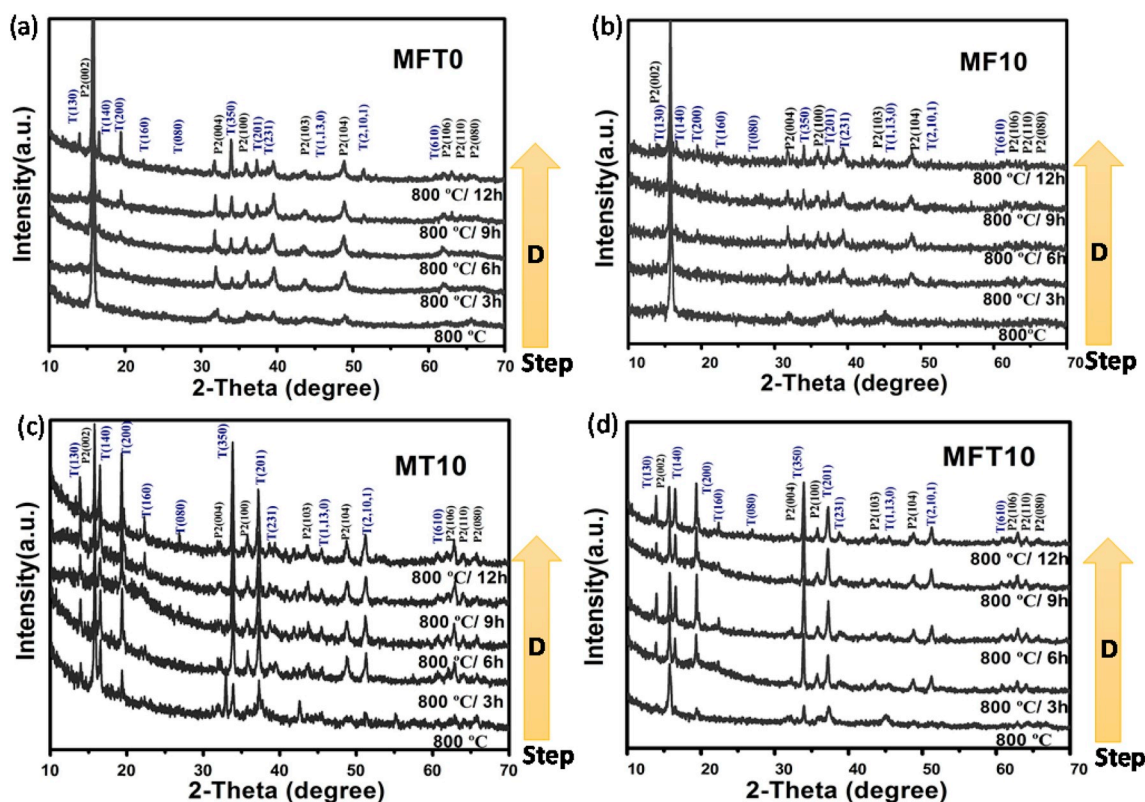


Fig. 5. (a–d) The ex-situ XRD patterns of MFT0, MF10, MT10 and MFT10 samples at 800°C calcination after quenching with liquid nitrogen. The calcination stages $800^\circ\text{C}/0\text{--}3\text{--}6\text{--}9\text{--}12\text{ h}$ are marked as step D.

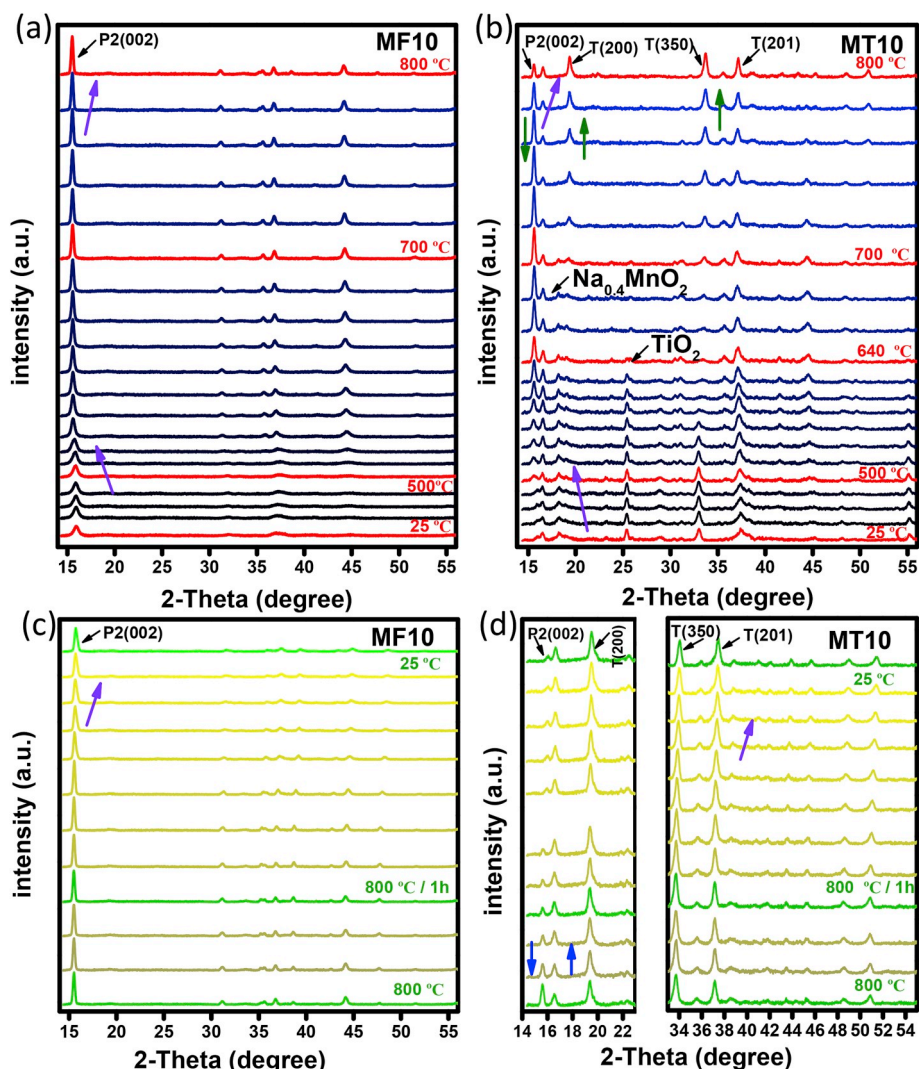


Fig. 6. In-situ high-temperature XRD patterns of the oxalate precursor MF10 and MT10 after pre-calcination (a–b) the heating process 25–500 °C at the heating rate of 5 °C/min and 500–800 °C at the slower heating rate of 1 °C/min for identifying the phase transitions (c–d) the constant temperature calcination stage 800 °C for 1 h and cooling process 800–25 °C at the rate of 5 °C/min.

To investigate the morphology evolution progress during calcination, SEM results of MF10 and MT10 were obtained by quenching the high-temperature state sample with liquid nitrogen (Fig. 7c–m). At the beginning of 800 °C, the MF10 (Fig. 7c–g) is composed of nano-sized polyhedral plate-like particles (~200 nm), in which almost no rod-shaped particles could be observed. When the holding time increased to 3 h, the plate-like particles grow larger (~2 μm) with increased thickness. And little rod-shaped tunnel structure particles also began to appear. Some nanoparticles (~500 nm) also remained. When calcined for 6 h, the plate-like and rod-like particles keep growing while the small particles further melt into larger particles, which is consistent with the corresponding XRD results. During the subsequent calcination period of 6–12 h, the particle surface gradually became smoother. As to MT10, more information about the growth of the tunnel structure can be obtained (Fig. 7h–m). At the beginning of 800 °C, the particles show severe agglomerates of nanoparticles (~400 nm). After 3 h, the length and width of the rod greatly developed with continued crystal growth. The rod-like particles with obvious edges and corners became more homogeneous corresponding to the enhanced crystallization. As for 6 h, the length of rod-like particles hardly changed but the width keep increasing. With the holding time increased to 9 h and longer 12 h, the particle with layer/tunnel were well-developed with no obvious difference in XRD patterns [49]. These results indicated that the particle size

and morphology are significantly affected by the high-temperature treatment at initial stage.

DFT calculations were performed to determine the relative stability between layer and tunnel structure before and after Fe³⁺/Ti⁴⁺ doping. For the pristine layer and tunnel structure (Fig. 8a), the tunnel structure is thermodynamically more stable than the layered structure by about 0.253 eV per MnO₂ unit. When one Ti and one Fe atom (simplified as one Fe–Ti pair) were introduced into the system, we found that the Ti⁴⁺ and Fe³⁺ prefer to locate at the neighboring Mn sites in the layered structure (Fig. 8b, left); while in the tunnel structure, the Fe³⁺ and Ti⁴⁺ prefer to replace the Mn2 and Mn3 site (Fig. 8b, right), respectively. The difference about the energetic trend between the layer and tunnel structure with the more composition of Fe³⁺/Ti⁴⁺ rapidly increased in Fig. 8d. This result indicated that the Ti⁴⁺ plays a key role on the thermal stability of layer/tunnel hybrid structures, which was consistent with XRD results.

3.2. Electrochemical evaluation

Galvanostatic charge/discharge tests were carried out to correlate the Fe³⁺/Ti⁴⁺ content, the layer/tunnel component ratio and the final electrochemical performance. As shown in Fig. 9a, the Fe-doped samples (MF5 and MF10) display higher capacity throughout the whole cycle

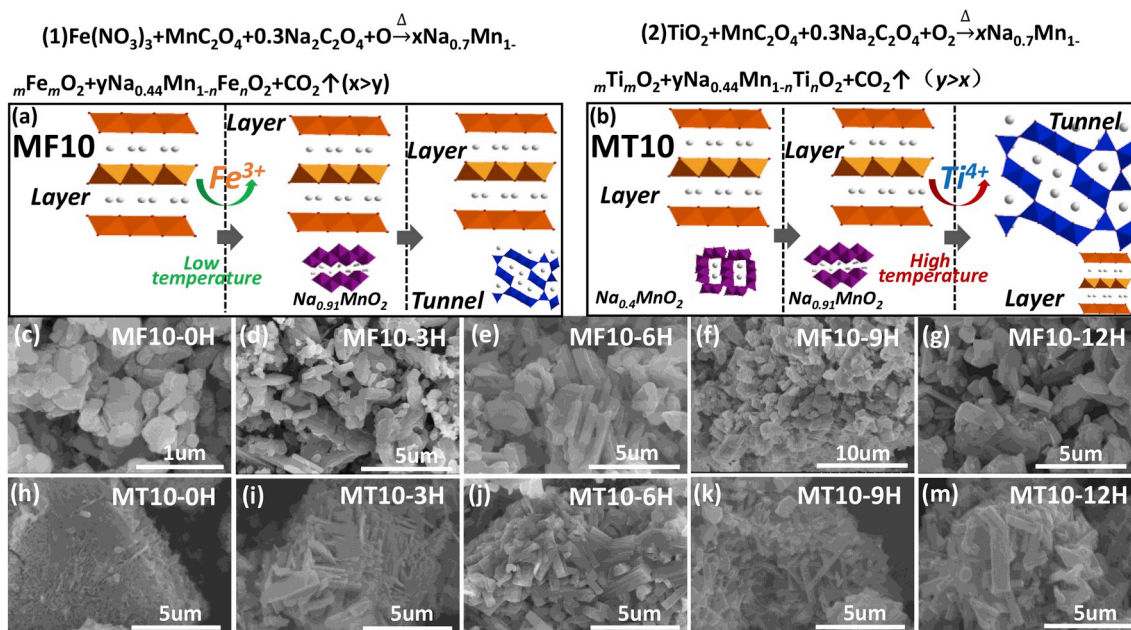


Fig. 7. The total reaction for the oxalate precursor (1) MF10 sample and (2) MT10 sample. The schematic diagram of composite structural formation progress of (a) MF10 and (b) MT10. SEM images of samples at 800 °C (0 h, 3 h, 6 h, 9 h, 12 h) after quenching with liquid nitrogen (c–g) MF10 sample (h–m) MT10 sample.

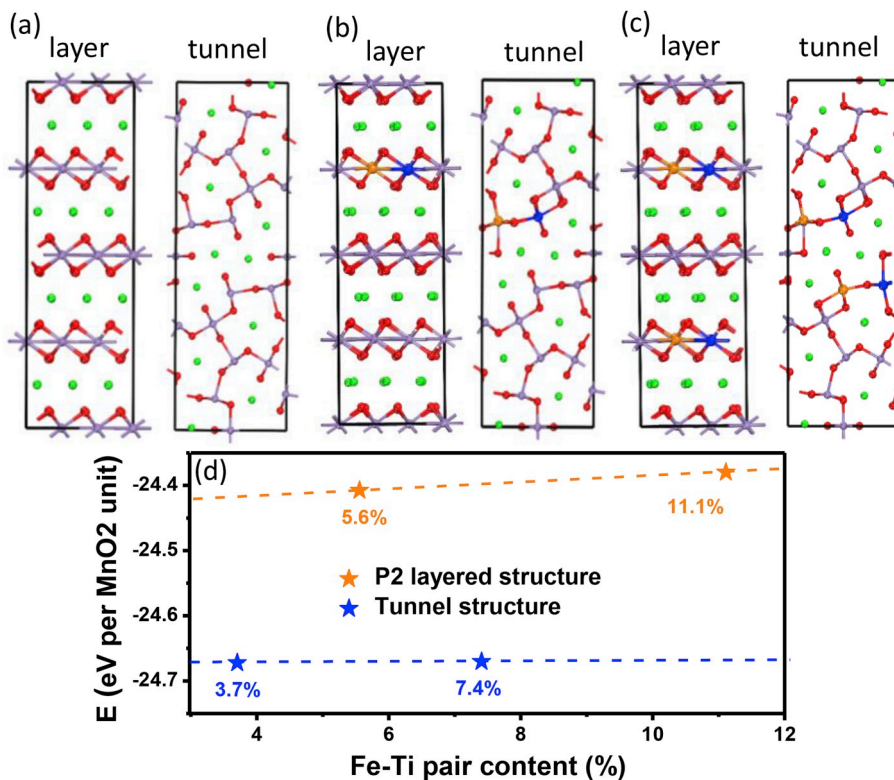


Fig. 8. Structural models of (a) pristine, (b) one Fe–Ti-pair, (c) two Fe–Ti-pair in layer (left) and tunnel (right) structures. Color modes: red for O, green for Na, purple for Mn, orange for Fe, and blue for Ti. (d) Total energies (E, in eV) per MnO₂ formula unit of the layered and tunnel structures with the increasing composition of Fe–Ti.

process compared with that of the pristine. More specifically, the MF5 and MF10 cathodes delivered initial discharge capacities of 140.4 and 132.1 mA h g⁻¹, which are higher than 128.1 mA h g⁻¹ of the pristine. That's due to the higher layer component after Fe-doping. Nevertheless, the excess Fe³⁺ entered the layered/tunnel composite may be detrimental due to the migration of Fe³⁺ into the Na layer of layered structure

during cycle [50,51]. The initial discharge capacities of Ti-doped samples with more tunnel structure component (MT5 and MT10) are lower than that of the pristine sample, which was related to lower theory capacity of tunnel structure. In addition, due to the excessive inactive Ti⁴⁺ reduced the content of active elements in the cathode material. Meanwhile, the MT5 and MT10 with more robust S-type Na + diffusion

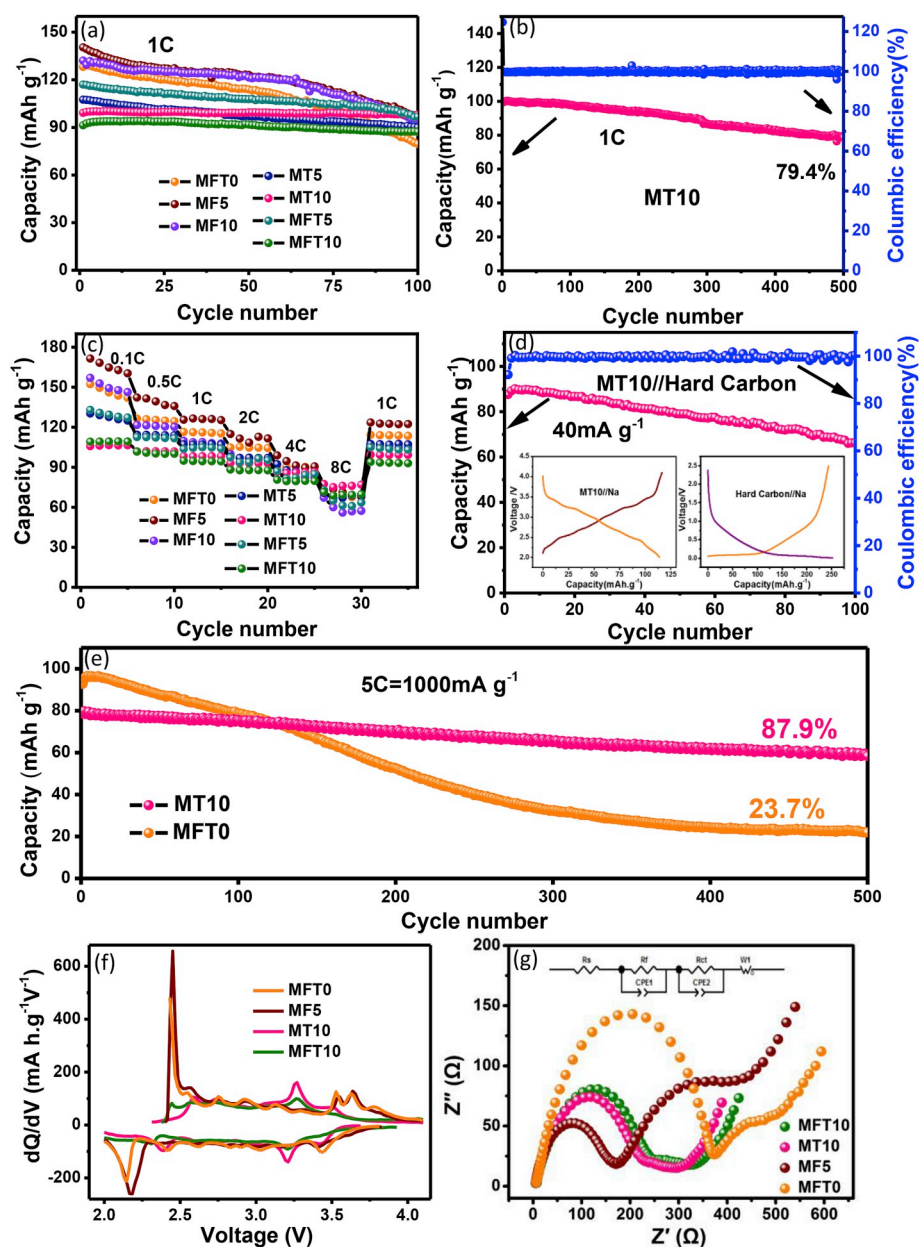


Fig. 9. Specific discharge capacities versus cycle number for 100 cycle at 1C (200 mA g^{-1}) in the potential of 2.0–4.1 V for each cathode (a) MFT0, MF5, MF10, MFT0, MT5, MT10, MFT0, MFT5 and MFT10. (b) The rate capability at different rates of 0.1C, 0.5C, 1C, 2C, 4C and 8C for each cathode (c) The long-term cycling performance of MT10 at 1C. (d) The full cell cycling performance of MT10 cathode at 40 mA g^{-1} in the potential of 1.5–3.5 V (e) Specific discharge capacities versus cycle number for 500 cycle at 5C (1000 mA g^{-1}) in the potential of 2.0–4.1 V for cathode MFT0 and MT10. (f) The corresponding dQ/dV plots for the 2nd cycle of MFT0, MF5, MT10 and MFT10 (g) EIS Impedance for the materials (MFT0, MF5, MT10, MFT10) after 3 cycles charge/discharge at 1C.

channel of tunnel structure exhibit better cycle stability. To be specific, the MT10 electrode maintained 78.7 mA h g^{-1} after 500 cycles, achieving a capacity retention of 79.4% (Fig. 9b). Encouragingly, MFT10 with more Fe/Ti co-doped shows the best cycling performance with high capacity retention of 94.5% and 86.1 mA h g^{-1} after 100 cycles, which refers the synergy effect of co-doping. This outstanding cycling stability was primarily attributed to the controlled synthesis and appropriate component ratio of layer/tunnel composite structures. In addition, the stronger bonding energy of Ti–O ($\Delta H_f, 298 \text{ K} = 662 \text{ kJ mol}^{-1}$) than that of Mn–O ($\Delta H_f, 298 \text{ K} = 402 \text{ kJ mol}^{-1}$) [33] also help to boost the cycle stability.

The enhanced rate performance further highlights the advantage of component ratio control of composite structures by varied Fe/Ti content (Fig. 9c). The MF5 showed higher discharge capacities of 171.5, 142.3, 125.6, 114.9, and 77.4 mA h g^{-1} from 0.1 to 8C ($1\text{C} = 200 \text{ mA g}^{-1}$), which was higher than that of MFT0. And MT10 delivered 77.4 mA h g^{-1} at 8C, approximately 72.6% of 0.1C, which is more superior to that of MFT0 (70.2 mA h g^{-1} corresponds to 46.1% of 0.1C). The MT10 cathode exhibited the superior high-rate cycle performance at 5C (1000 mA g^{-1})

with a capacity retention of 87.9% after 500 cycles (Fig. 9e), which is much better than that of MFT0 (23.7%). Furthermore, MFT10 electrode demonstrated similar performance of MT10 sample. These results of MF10, MT10 and MFT10 indicated that Ti played a more important role in Mn-based layered-tunnel composite structure. The Symmetric cell, which was assembled with MT10//hard carbon after pre-cycled for 3 cycles, demonstrated an initial capacity of 87.6 mA h g^{-1} in the potential range 1.5–3.5 V at 40 mA g^{-1} with of 75.7% maintained after 100 cycles. As discussed above, the as-fabricated materials with the overwhelming structural superiority undoubtedly promise the advantages of multiple design strategy for composite structure materials.

The charge/discharge curves of MFT0/MF5/MT10/MFT10 cathode were presented in Figs. S5a–d. Although MF5 electrode with added layer structures reached the higher discharge special capacity, unfortunately, the cyclic stability is worse owing to the structural instability. Note that the charge/discharge profiles of MT10/MFT10 cathodes overlap well, implying excellent reversibility and small polarization (Fig. S6c). The detailed Na + insertion and extraction steps can be observed from the second dQ/dV profile in Fig. 9f. The prominent redox couple 2.2/2.4 V is

related to $\text{Mn}^{3+}/\text{Mn}^{4+}$ redox process in MFT0. The series of small peaks in the higher voltage range of 2.5–3.3 V are associated with the Na^+ /vacancy ordering arrangement during Na + extraction/reinsertion and the electrostatic repulsion among Na3, Na2, and Na1 sites in tunnel structure [27]. The small redox peaks disappeared in MF5 dQ/dV profile, which is consistent with more layered structure. The $\text{Mn}^{3+}/\text{Mn}^{4+}$ redox peak (2.2/2.4 V) with higher intensity can be observed in MF5. And the 3.4/3.7 V redox couple is related with the fewer $\text{Fe}^{3+}/\text{Fe}^{4+}$ [52]. The MT10/MFT10 cathodes show different Na + extraction/insertion behaviors assigned to the increased tunnel structure (Fig. 9f). The multi peaks in the dQ/dV curve indicated the extraction of Na^+ from different sites, which was similar with that of tunnel structure [37,53,54].

Fig. 9g shows the Nyquist plots of MFT0, MT10, MF5 and MFT10 at the discharged state of 2.0 V after 3 cycles at 1C. And equivalent circuit for the fitting is presented in the inset. The curves of all samples were composed of two semicircles in the high frequency and a slope in the low-frequency region [52]. The first semicircle in the high frequency region is related to the migration of Na + through a surface layer formed in the electrode (R_f). Another semicircle in the middle-frequency region, corresponds to the charge transfer resistance at the electrode/electrolyte interface (R_{ct}). Obviously, by comparing the diameters of the semicircles, the initial R_f values of MFT0, MT10, MF5 and MFT10 electrodes were found to be 388.7, 223.2, 161.6 and 234.4 Ω , respectively. Moreover, the R_{ct} values of MFT0, MT10, MF5 and MFT10 were 243.7, 110.7, 328.2 and 83.3 Ω , respectively. These results indicated that the MT10 and MFT10 electrode demonstrated lower impedance with the increased ratio of tunnel structure after more composition of Ti^{4+} . However, R_f of MF5 was smaller than MFT0 and the (R_{ct}) of MF5 was bigger than MFT0 with the increase in the component ratio of the P2 structure with more composition of Fe^{3+} .

The sloping line at the low-frequency region can be ascribed to the Warburg diffusion process (Z_w), which is associated with Na + diffusion in the electrode. The Na + diffusion coefficient (D_{Na^+}) was calculated to evaluate the kinetics for the prepared electrodes according to the following equation:

$$D_{\text{Na}^+} = R^2 T^2 / (2A^2 n^4 F^4 C^2 \sigma^2)$$

Here, R is the gas constant (8.314 J K⁻¹ mol⁻¹), T is the absolute temperature (298.15 K), A is active surface area of the electrode, n is the number of the electrons per molecule during oxidization, F is the Faraday constant (96 500 C mol⁻¹), C can be Na + concentration in the cathode calculated from the density and the molecular weight of the materials synthesized by different methods, and σ is the Warburg coefficient, it can be decided from the chart of $Z' - \omega^{-1/2}$ in the low frequency region. The Warburg coefficient σ can be calculated by the equation:

$$Z_{re} = R_f + R_{ct} + \sigma \omega^{-1/2}$$

Where the R_f is the resistance of electrolyte, R_{ct} is the charge transfer resistance, and ω is the angular frequency in the low frequency region. Both R_f and R_{ct} were kinetics parameters independent of frequency. Therefore, the Warburg factor can be obtained from the slope between Z_{re} and the inverse square root of the angular frequency ($\omega^{-1/2}$), as shown in Fig. S6. Moreover, the calculated Na + diffusion coefficients of the sample MFT0, MT10, MF5 and MFT10 were determined to be 2.01×10^{-13} , 5.48×10^{-13} , 1.11×10^{-13} , and 4.9×10^{-13} cm² s⁻¹. An enhancement of electrochemical kinetic characteristics has been achieved from the increasing ratio of tunnel structure with more Ti^{4+} . These results shown that the varied content of $\text{Fe}^{3+}/\text{Ti}^{4+}$ and the regulation of structure component ratio markedly affected the charge transfer resistance and Na + diffusion coefficients, which keep in good accordance with the distinctive electrochemical performances.

4. Conclusions

In summary, series of Fe/Ti doped $\text{Na}_{0.6}\text{Mn}_{1-x-y}\text{Fe}_x\text{Ti}_y\text{O}_2$ ($x = 0, 0.05, 0.1, y = 0, 0.05, 0.1$) with varied component ratios of layer-tunnel composite were successfully synthesized. The investigation of the structure formation process during calcination demonstrated that the layered structure can be formed in the lower temperature range, the crystal structure and particle grown in the higher temperature stage. And the transformation of layer to tunnel structure and the particle morphology change were mainly happened in the high-temperature section. The Fe/Ti migration into the host structure at low-temperature/high-temperature hindered/promoted the structure transition and affected component ratio in final products. The Ti^{4+} played the dominant role to result in more tunnel structures with Fe/Ti co-doping, which was also validated by DFT calculation. The component ratio of layer/tunnel composite structures can be directionally regulated by appropriate adjustment of Fe/Ti content for the controllable electrochemical properties. The research grasps new insight into the relationship of the different ion-doping, hybrid structural formation progress and electrochemical synergistic effect of $\text{Na}_{0.6}\text{Mn}_{1-x-y}\text{Fe}_x\text{Ti}_y\text{O}_2$ cathodes for SIBs. We hope that this study could inspired us to investigate and control the material structure formation process with different ion for rationally designing and intelligently tuning the final products with desired electrochemical properties.

Declaration of competing interest

The authors declare that they have no known competing financial interests or personal relationships that could have appeared to influence the work reported in this paper.

Acknowledgments

This work was supported by the National Natural Science Foundation of China (Grant Nos. 21805198, 21878195, 21805018 and U1909213), Distinguished Young Scholars of Sichuan University (2017SCU04A08), Huohua Ku project of Sichuan University (2018SCUH0094), Research Foundation for the Postdoctoral Program of Sichuan University (2018SCU12045), and Research Foundation for the Sichuan University and Zigong City Joint research project (2018CDZG-16). The authors also acknowledge the support provided by the Natural Sciences and Engineering Research Council of Canada (NSERC), University of Waterloo, Waterloo Institute for Nanotechnology. We thank Dr Zhuo Zheng for help with data analysis.

Appendix A. Supplementary data

Supplementary data to this article can be found online at <https://doi.org/10.1016/j.nanoen.2020.104539>.

References

- [1] C. Delmas, *Adv. Energy Mater.* 8 (2018) 1703137–1703145.
- [2] R.J. Clément, P.G. Bruce, C.P. Grey, *J. Electrochem. Soc.* 162 (2015) A2589–A2604.
- [3] Q. Liu, Z. Hu, M. Chen, C. Zou, H. Jin, S. Wang, S.L. Chou, S.X. Dou, *Small* (2019) 1805381–1805404.
- [4] Y.-P. Deng, Y. Jiang, D. Luo, J. Fu, R. Liang, S. Cheng, Z. Bai, Y. Liu, W. Lei, L. Yang, J. Zhu, Z. Chen, *ACS Energy Lett* 2 (2017) 2706–2712.
- [5] Y.P. Deng, Z.W. Yin, Z.G. Wu, S.J. Zhang, F. Fu, T. Zhang, J.T. Li, L. Huang, S. G. Sun, *ACS Appl. Mater. Interfaces* 9 (2017) 21065–21070.
- [6] L. Zou, J. Li, Z. Liu, G. Wang, A. Manthiram, C. Wang, *Nat. Commun.* 10 (2019) 3447–3456.
- [7] Y. Wang, X. Wang, X. Li, R. Yu, M. Chen, K. Tang, X. Zhang, *Chem. Eng. J.* 360 (2019) 139–147.
- [8] Y. Wen, J. Fan, C. Shi, P. Dai, Y. Hong, R. Wang, L. Wu, Z. Zhou, J. Li, L. Huang, S.-G. Sun, *Nano Energy* 60 (2019) 162–170.
- [9] L. Yang, X. Li, J. Liu, S. Xiong, X. Ma, P. Liu, J. Bai, W. Xu, Y. Tang, Y.Y. Hu, M. Liu, H. Chen, *J. Am. Chem. Soc.* 141 (2019) 6680–6689.

- [10] Q. Zhao, Z. Guo, L. Wang, Y. Wu, F.K. Butt, Y. Zhu, X. Xu, X. Ma, C. Cao, ACS Appl. Mater. Interfaces (2019) 30819–30827.
- [11] W.M. Dose, N. Sharma, J.C. Pramudita, H.E.A. Brand, E. Gonzalo, T. Rojo, Chem. Mater. 29 (2017) 7416–7423.
- [12] Q. Yang, P.F. Wang, J.Z. Guo, Z.M. Chen, W.L. Pang, K.C. Huang, Y.G. Guo, X. L. Wu, J.P. Zhang, ACS Appl. Mater. Interfaces 10 (2018) 34272–34282.
- [13] Y. Pei, Q. Chen, Y.-C. Xiao, L. Liu, C.-Y. Xu, L. Zhen, G. Henkelman, G. Cao, Nano Energy 40 (2017) 566–575.
- [14] W. Hua, M. Chen, B. Schwarz, M. Knapp, M. Bruns, J. Barthel, X. Yang, F. Sigel, R. Azmi, A. Senyshyn, A. Missiul, L. Simonelli, M. Etter, S. Wang, X. Mu, A. Fiedler, J.R. Binder, X. Guo, S. Chou, B. Zhong, S. Indris, H. Ehrenberg, Adv. Energy Mater. 9 (2019) 1803094–1803103.
- [15] D. Wang, R. Kou, Y. Ren, C.J. Sun, H. Zhao, M.J. Zhang, Y. Li, A. Huq, J.Y.P. Ko, F. Pan, Y.K. Sun, Y. Yang, K. Amine, J. Bai, Z. Chen, F. Wang, Adv. Mater. 29 (2017) 1606715–1606722.
- [16] Y.-N. Zhou, P.-F. Wang, Y.-B. Niu, Q. Li, X. Yu, Y.-X. Yin, S. Xu, Y.-G. Guo, Nano Energy 55 (2019) 143–150.
- [17] Z. Yan, L. Tang, Y. Huang, W. Hua, Y. Wang, R. Liu, Q. Gu, S. Indris, S.L. Chou, Y. Huang, M. Wu, S.X. Dou, Angew. Chem. Int. Ed. 58 (2019) 1412–1416.
- [18] D. Wang, H. Chen, X. Zheng, L. Qiu, J. Qu, Z. Wu, Y. Zhong, W. Xiang, B. Zhong, X. Guo, ChemElectroChem (2019) 5155–5161.
- [19] S. Guo, P. Liu, H. Yu, Y. Zhu, M. Chen, M. Ishida, H. Zhou, Angew. Chem. Int. Ed. 54 (2015) 5894–5899.
- [20] Z.-Y. Li, J. Zhang, R. Gao, H. Zhang, L. Zheng, Z. Hu, X. Liu, J. Phys. Chem. C 120 (2016) 9007–9016.
- [21] E. Lee, J. Lu, Y. Ren, X. Luo, X. Zhang, J. Wen, D. Miller, A. DeWahl, S. Hackney, B. Key, D. Kim, M.D. Slater, C.S. Johnson, Adv. Energy Mater. 4 (2014) 1400458–1400465.
- [22] Y. Xiao, P.-F. Wang, Y.-X. Yin, Y.-F. Zhu, X. Yang, X.-D. Zhang, Y. Wang, X.-D. Guo, B.-H. Zhong, Y.-G. Guo, Adv. Energy Mater. 8 (2018) 1800492–1800498.
- [23] Z.G. Wu, J.T. Li, Y.J. Zhong, X.D. Guo, L. Huang, B.H. Zhong, D.A. Agyeman, J. M. Lim, D.H. Kim, M.H. Cho, Y.M. Kang, ACS Appl. Mater. Interfaces 9 (2017) 21267–21275.
- [24] H. Su, H. Yu, Small Methods 3 (2018) 1800205–1800219.
- [25] Y.P. Deng, Z.G. Wu, R. Liang, Y. Jiang, D. Luo, A. Yu, Z. Chen, Adv. Funct. Mater. 29 (2019) 1808522–1808545.
- [26] G.-L. Xu, R. Amine, Y.-F. Xu, J. Liu, J. Gim, T. Ma, Y. Ren, C.-J. Sun, Y. Liu, X. Zhang, S.M. Heald, A. Solhy, I. Saadoun, W.L. Mattis, S.-G. Sun, Z. Chen, K. Amine, Energy Environ. Sci. 10 (2017) 1677–1693.
- [27] T.R. Chen, T. Sheng, Z.G. Wu, J.T. Li, E.H. Wang, C.J. Wu, H.T. Li, X.D. Guo, B. H. Zhong, L. Huang, S.G. Sun, ACS Appl. Mater. Interfaces 10 (2018) 10147–10156.
- [28] J. Qu, T. Sheng, Z.-g. Wu, T.-r. Chen, H. Chen, Z.-g. Yang, X.-d. Guo, J.-t. Li, B.-h. Zhong, X.-s. Dou, J. Mater. Chem. A 6 (2018) 13934–13942.
- [29] F. Fu, P. Liu, H. Wang, Mater. Lett. (2019) 124–127.
- [30] G.S. Shinde, P.D. Nayak, S.P. Vanam, S.K. Jain, A.D. Pathak, S. Sanyal, J. Balachandran, P. Barpanda, J. Power Sources 416 (2019) 50–55.
- [31] W. Kang, Z. Zhang, P.-K. Lee, T.-W. Ng, W. Li, Y. Tang, W. Zhang, C.-S. Lee, D. Y. Wai Yu, J. Mater. Chem. A 3 (2015) 22846–22852.
- [32] W. Kang, D.Y. Yu, P.K. Lee, Z. Zhang, H. Bian, W. Li, T.W. Ng, W. Zhang, C.S. Lee, ACS Appl. Mater. Interfaces 8 (2016) 31661–31668.
- [33] R. Dang, M. Chen, Q. Li, K. Wu, Y.L. Lee, Z. Hu, X. Xiao, ACS Appl. Mater. Interfaces 11 (2019) 856–864.
- [34] T. Yamashita, P. Hayes, Appl. Surf. Sci. 254 (2008) 2441–2449.
- [35] T.-R. Chen, Z.-G. Wu, W. Xiang, E.-H. Wang, C.-J. Wu, M.-Z. Chen, X.-D. Guo, B.-H. Zhong, Ceram. Int. 43 (2017) 6303–6311.
- [36] S. Demirel, E. Oz, E. Altin, S. Altin, A. Bayri, P. Kaya, S. Turan, S. Avci, Mater. Char. 105 (2015) 104–112.
- [37] D. Zhang, W.-j. Shi, Y.-w. Yan, S.-d. Xu, L. Chen, X.-m. Wang, S.-b. Liu, Electrochim. Acta 258 (2017) 1035–1043.
- [38] S. Bao, S.H. Luo, Z.Y. Wang, S.X. Yan, Q. Wang, J. Colloid Interface Sci. 544 (2019) 164–171.
- [39] F. Hu, M.M. Doeff, J. Power Sources 129 (2004) 296–302.
- [40] A. Eftekhari, M. Kazemzad, F. Moztaaradeh, Mater. Res. Bull. 40 (2005) 2205–2211.
- [41] S. Liu, C.-Z. Fan, Y. Zhang, C.-H. Li, X.-Z. You, J. Power Sources 196 (2011) 10502–10506.
- [42] L. Mai, H. Li, Y. Zhao, L. Xu, X. Xu, Y. Luo, Z. Zhang, W. Ke, C. Niu, Q. Zhang, Sci. Rep. 3 (2013) 1718–1725.
- [43] M. Xu, Y. Niu, Y. Li, S. Bao, C.M. Li, RSC Adv. 4 (2014) 30340–30345.
- [44] Q. Chu, X. Wang, B. Li, H. Jin, X. Cao, X. Zhao, X. Liu, J. Cryst. Growth 322 (2011) 103–108.
- [45] C. Liu, W.-l. Guo, Q.-h. Wang, J.-g. Li, X.-P. Yang, J. Alloys Compd. 658 (2016) 588–594.
- [46] H. Yang, H.H. Wu, M. Ge, L. Li, Y. Yuan, Q. Yao, J. Chen, L. Xia, J. Zheng, Z. Chen, J. Duan, K. Kisslinger, X.C. Zeng, W.K. Lee, Q. Zhang, J. Lu, Adv. Funct. Mater. 29 (2019) 1808825–1808837.
- [47] M. Jayakumar, K. Hemalatha, K. Ramesha, A.S. Prakash, Phys. Chem. Chem. Phys. 17 (2015) 20733–20740.
- [48] S. Xu, Y. Wang, L. Ben, Y. Lyu, N. Song, Z. Yang, Y. Li, L. Mu, H.-T. Yang, L. Gu, Y.-S. Hu, H. Li, Z.-H. Cheng, L. Chen, X. Huang, Adv. Energy Mater. 5 (2015) 1501156–1501164.
- [49] L.G. Chagas, D. Buchholz, C. Vaalma, L. Wu, S. Passerini, J. Mater. Chem. A 2 (2014) 20263–20270.
- [50] W.M. Dose, N. Sharma, J.C. Pramudita, M. Avdeev, E. Gonzalo, T. Rojo, Chem. Mater. 30 (2018) 7503–7510.

- [51] Y. Li, Y. Gao, X. Wang, X. Shen, Q. Kong, R. Yu, G. Lu, Z. Wang, L. Chen, Nano Energy 47 (2018) 519–526.
- [52] Y. Bai, L. Zhao, C. Wu, H. Li, Y. Li, F. Wu, ACS Appl. Mater. Interfaces 8 (2016) 2857–2865.
- [53] X. Zhou, R.K. Guduru, P. Mohanty, J. Mater. Chem. A 1 (2013) 2757–2761.
- [54] B. Fu, X. Zhou, Y. Wang, J. Power Sources 310 (2016) 102–108.



Dong Wang is currently a graduate student in the school of Chemical Engineering at Sichuan University. His research focuses on the cathode materials for high performance sodium-ion batteries.



ChenGuang Shi received his B.S. degree from Xiamen University in 2016. He is pursuing his Ph.D. degree in Xiamen University and his current research interest is focused mainly on cathode materials and electrolytic additives for lithium-ion batteries.



Ya-Ping Deng received his Master's degree (2016) in Xiamen University with Prof. Shi-Gang Sun. He is now pursuing his Ph. D. in Chemical Engineering under the supervision of Prof. Zhongwei Chen at University of Waterloo. His research currently focusses on the exploration of novel electrode materials and solid-state electrolytes for lithium-ion batteries and rechargeable metal-air batteries.



Zhenguo Wu obtained his Ph.D. (2016) from the Sichuan University with Prof. Ben-He Zhong. He is currently an associate researcher at Sichuan University. His research interests include the development of advanced energy materials for lithium-ion and sodium ion batteries.



Zuguang Yang is currently a Ph.D. in the school of Chemical Engineering at Sichuan University. He received his master degree in 2017 from Sichuan University. His research focus on the anode materials for high performance sodium-ion battery and study their sodium-ions storage mechanisms.



Ling Huang received his Ph.D. degree from the Department of Chemistry of Xiamen University in 1997. He has worked in Xiamen University from 2000 to date. He is now a professor of chemistry at Xiamen University, and his research interests include synthesis of tin based alloys by electrochemical deposition and high-energy cathode materials of lithium ion batteries.



Yanjun Zhong received her Ph.D. (2015) from the Sichuan University with Prof. Ben-He Zhong. She is now an assistant research fellow at Sichuan University. Her research is currently focused on the exploration of novel electrode materials for lithium-ion batteries and sodium-ion batteries.



Xiaodong Guo is currently a professor in the School of Chemical Engineering of Sichuan University, visiting professor in university of Wollongong of Australia. He hosted National Natural youth projects, Surface project, Sichuan Science and Technology Support Plan, enterprise horizontal projects, etc, and participated in 863 national projects, National Key R&D Program of China, etc. He has published over 100 papers in *Angew. Chem.*, *Int. Ed. Adv. Mater.*, *Adv. Energy. Mater.* and *Adv. Sci.* etc. by the first author/ Corresponding author.



Yi Jiang received her Ph.D. degree from the National Center for Nanoscience and Technology, University of Chinese Academy Science in 2018. Currently, she works as a postdoctoral research fellow under supervisor of Prof. Zhongwei Chen at the University of Waterloo. Her research interests focus on the development of metal-organic framework based nano-structured electrode materials for rechargeable metal-air batteries.



Dr. Zhongwei Chen is Canada Research Chair Professor in Advanced Materials for Clean Energy at University of Waterloo, fellow of the Royal Society of Canada and fellow of the Canadian Academy of Engineering. His research interests are in the development of advanced energy materials for metal-air batteries, lithium ion batteries and fuel cells. He has published 1 book, 7 book chapters and more than 300 peer reviewed journal articles with over 28 000 citations with H-index 81 (Google Scholar). He is also listed as inventor on 15 US/international patents, with several licensed to companies in USA and Canada. He was recipient of the 2016 E. W. R Steacie Memorial Fellowship, which followed shortly upon several other prestigious honors, including the Ontario Early Researcher Award, an NSERC Discovery Supplement Award, the Distinguished Performance and the Research Excellence Awards from the University of Waterloo.



Benhe Zhong obtained her bachelor's degree (1955) from Chengdu institute of technology (Chengdu university of science and technology in the past, integrated into sichuan university). She is a distinguished professor of Sichuan university and a top scientist in the field of phosphorus chemical engineering. She has conducted studies on the basic and industrialization for clean processing and comprehensive utilization of phosphorus resources for about 60 years and gained series of major achievements. In recent years, her research interests involve the development of advanced energy materials and electrodes for lithium-ion batteries, sodium-ion batteries and lithium-sulphur batteries.